Journal of Marine Science and Application (2026) 25: 122-135
https://doi.org/10.1007/s11804-025-00776-4

RESEARCH ARTICLE

Numerical Simulation of the Welding Deformation of Marine Thin Plates Based on a Temperature Gradient–thermal Strain Method

Lin Wang[1], Yugang Miao[1*], Zhenjian Zhuo[2], Chunxiang Lin[2], Benshun Zhang[3] and Duanfeng Han[1]

Received: 20 November 2024 / Accepted: 20 August 2025

Abstract

Marine thin plates are susceptible to welding deformation owing to their low structural stiffness. Therefore, the efficient and accurate prediction of welding deformation is essential for improving welding quality. The traditional thermal elastic-plastic finite element method (TEP-FEM) can accurately predict welding deformation. However, its efficiency is low because of the complex nonlinear transient computation, making it difficult to meet the needs of rapid engineering evaluation. To address this challenge, this study proposes an efficient prediction method for welding deformation in marine thin plate butt welds. This method is based on the coupled temperature gradient-thermal strain method (TG-TSM) that integrates inherent strain theory with a shell element finite element model. The proposed method first extracts the distribution pattern and characteristic value of welding-induced inherent strain through TEP-FEM analysis. This strain is then converted into the equivalent thermal load applied to the shell element model for rapid computation. The proposed method—particularly, the gradual temperature gradient-thermal strain method (GTG-TSM)—achieved improved computational efficiency and consistent precision. Furthermore, the proposed method required much less computation time than the traditional TEP-FEM. Thus, this study lays the foundation for future prediction of welding deformation in more complex marine thin plates.

Keywords Marine thin plate; Welding deformation; Numerical simulation; Temperature gradient-thermal strain method; Shell element

1 Introduction

With the growing focus on environmental protection, ship development is increasingly emphasizing lightweight and green technologies. Thin plates, valued for their lightness and formability, are being used more extensively in shipbuilding. Welding is the primary method for joining thin plate structures when assembling a ship (Mancini et al., 2021; Doan and Zden, 2021). However, these plates have low stiffness, making them susceptible to welding-induced deformation, which can alter the shape and dimensions of the welded components (Qiu et al., 2023). Excessive deformation can compromise structural accuracy and safety in shipbuilding, resulting in higher costs and longer manufacturing times because of the need for manual corrections. Therefore, accurately predicting welding deformation in marine thin plates is essential for enhancing shipbuilding quality and reducing construction time (Azad et al., 2020; Woo and Kitamura, 2022).

With the continuous advancement of computer hardware and finite element software, numerical simulation technology has become an increasingly vital tool in analyzing welding deformation. This technology is now indispensable for investigating structural deformations during welding. The two primary numerical methods for simulating welding deformation are the thermal elastic-plastic finite element method (TEP-FEM) and the inherent strain method (ISM) (Battista et al., 2024; Shoor et al., 2024; Hashemzadeh et al., 2022). The TEP-FEM, pioneered by Professor Ueda at Osaka University, Japan, was developed to address the practical challenges associated with welding deformation (Ueda and Yamakawa, 1971). This method can track temperature variations and the stress-strain state of the weld by incrementally computing the residual stress and defor-

Article Highlights

- The temperature gradient-thermal strain method is proposed to simulate the welding deformation in marine thin plates.
- The proposed method, combined with a shell element finite element model, simulates saddle-shaped deformation trends.
- The gradual temperature gradient-thermal strain method (GTG-TSM) closely matches the actual residual plastic strain generation process.
- The GTG-TSM has high computational accuracy and efficiency in predicting welding deformation.

✉ Yugang Miao
miaoyg@hrbeu.edu.cn

[1] National Key Laboratory of Science and Technology on Underwater Vehicle, Harbin Engineering University, Harbin 150001, China

[2] CSSC Huangpu Wenchong Shipbuilding Company Limited, Guangzhou 511462, China

[3] Jiangsu Automation Research Institute, Lianyungang 222006, China

mation. That is, it can simulate the stress-strain condition at any moment in welding. By using a specified time step, this method calculates the welding temperature field at each moment, and it computes the stress and strain increments induced by temperature changes over time, ultimately resulting in accumulated residual stress and deformation (Hashemzadeh et al., 2022; Ueda and Yamakawa, 1971). Many studies have successfully explored similar welding problems using TEP-FEM. For example, Gannon et al. (2016) and Farajkhah et al. (2017) combined the TEP-FEM with a 3D solid finite element model to analyze the deformations generated when welding stiffened plates with steel plates. They evaluated the behavior of 14 stiffened plates under axial compressive loads with welding-induced residual stresses. Additionally, the method was applied to analyze the welding processes of 6061-T6 Al alloy plates to thoroughly compare the thermal and mechanical results of the two welding techniques. Nishimura et al. (2021) utilized the TEP-FEM to numerically simulate the welding deformation in the lap joints of alloy steel. They verified that the numerical model, which accounts for thermal softening behavior, provides more accurate analysis results. Su et al. (2023) used TEP-FEM to analyze the welding deformations of Invar steel cross joints under different welding sequence schemes and determined the optimal welding-deformation control scheme. Although TEP-FEM can theoretically analyze welding stress and deformation in any complex structures, it has considerable drawbacks, such as substantial computational demands and prolonged calculation times. The high computational costs and lengthy processing duration of the method limit its application to the deformation calculation of complex welded plates (Honaryar et al., 2020; Wang et al., 2020)

To address the computational inefficiency of the TEP-FEM in this field, Murakawa et al. (2009) and Ueda et al. (1993) proposed the inherent strain method (ISM) that eliminates the inefficiency of the traditional thermal elastic-plastic analyses. The ISM focuses on analyzing the weld strain after welding, rather than tracking the entire welding process. The crux of this method lies in investigating the relationship between inherent strain and factors such as welding parameters and weldment dimensions. These inherent strains are used as the initial strain values and loaded onto the corresponding areas; then, the residual stresses and deformations of the entire weldment are analyzed via a one-time elastic finite element calculation. This method significantly reduces computational complexity and time consumption, thereby enhancing the analysis efficiency (Honaryar et al., 2020; Ueda et al., 1993; Ueda and Yuan, 1992; Liang et al., 2024). Currently, the ISM is widely used to predict welding deformations in complex structures. For instance, Lu et al. (2019) numerically simulated the deformation of a single-sided welded T-joint by using ISM and TEP-FEM and compared the results of the two methods. They validated that the ISM results agreed with the TEP-FEM results. Subsequently, ISM was applied to simulate the welding deformation of a bogie frame, demonstrating the ability of ISM to predict welding deformations of such structures. Wang et al. (2020) applied ISM to predict plane welding deformations in torsion box structures, the two key structures of a 2000TEU ultralarge container ship. The simulation results were in close agreement with the measured results. Honaryar et al. (2020) simulated the welding deformation in an aluminum catamaran using ISM and validated the results.

Although ISM has been successfully used to predict plate structure deformation, this study found that the classic ISM has certain limitations in analyzing the deformation of thin plate structures during welding (Liang et al., 2024; Wu and Kim, 2020). For instance, it does not account for the welding direction in such structures, and it overlooks the fact that in a real deformation process, the molten weld pool will gradually solidify and shrink due to the thermal radiation during welding, causing welding deformation. This results in discrepancies between the ISM-predicted and actual welding deformation in thin plate welds. In this regard, the shell element finite element model has the advantages that it requires fewer elements and facilitates easier model establishment than the solid finite element model when describing the same structure. Therefore, combining the ISM with the shell element model to efficiently and precisely predict the thin plate deformation is an important research topic.

This study investigates the butt welding of AH36 marine thin plates by using the commercial finite element software SYSWELD as the computational platform. First, a nonlinear transient analysis of AH36 marine thin plate butt welding deformation was conducted using TEP-FEM in combination with a 3D solid finite element model. The results were validated against experimental data to extract the inherent strain. Subsequently, two temperature gradient-thermal strain methods based on inherent strain theory were proposed and applied along with a shell element finite element model to linearly compute the welding deformation in the same structure. The results show that the proposed gradual temperature gradient-thermal strain method (GTG-TSM) provides deformation predictions consistent with the experimental and TEP-FEM results while significantly reducing the computation time. Thus, the proposed approach is an effective solution for efficiently and accurately predicting welding deformation in complex thin-walled structures.

2 Experimental material and method

2.1 Experimental material and welding process

This study utilized AH36 marine thin steel plates, which

exhibit good weldability, high strength, and excellent corrosion resistance. Tables 1 and 2 summarize its composition and performance information. During the experiment, butt welding of AH36 marine thin steel plates was performed by the flux-cored wire CO_2 gas shielded welding (abbreviation: FCAW) process. The welding wire used had a diameter of 1.2 mm (designation: Supecored 71). The welding process parameters are summarized in Table 3. The dimensions of the experimental plates are shown in Figure 1, with individual plate dimensions of 300 mm × 100 mm × 3 mm. Here L_1 represents longitudinal path and T_1, T_2 and T_3 represent transverse paths. Prior to full welding, tack welding was applied to fix the plates, and no external constraints were applied during full welding.

Table 1 Composition of AH36 marine thin steel plate (wt%)

Element	Percentage by mass	Element	Percentage by mass
C	0.1600	Nb	0.0180
Si	0.2200	V	0.0010
Mn	1.1600	Ti	0.0160
P	0.0140	Ni	0.0200
S	0.0052	Cu	0.0400
Als	0.0300	Ceg	0.3700
Cr	0.0400		

Table 2 Mechanical performances of the AH36 marine thin steel plate

Yield strength (MPa)	Tensile strength (MPa)	Elongation (%)	Hardness (HV)	Impact energy (J)
⩾355	522	41.5	182	157

Table 3 Welding experiment parameters

Welding method	Welding current (A)	Welding voltage (V)	Welding speed (mm/s)	Welding wire diameter (mm)
FCAW	140	22	2	1.2

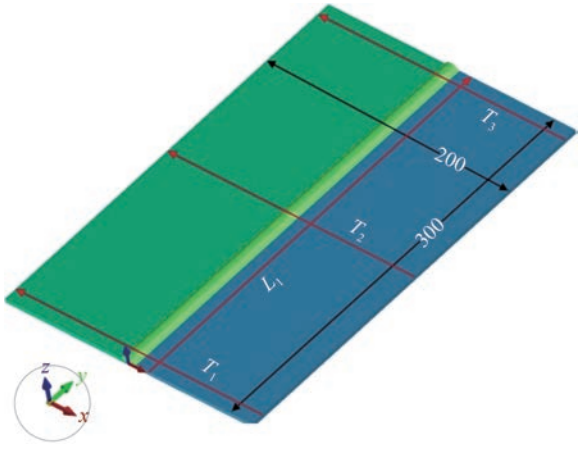

Figure 1 Structure and dimensions of the marine thin plate butt weld (unit: mm)

2.2 Temperature field monitoring during welding and postwelding deformation measurement

A K-type thermocouple multi-channel temperature recorder (Figure 2) was used to record the thermal data and to prove the accuracy of the model and simulated temperature field. Two channels captured thermal cycle data at the detection points shown in Figure 3. Points K_1 and K_2 were located on one side of the plate in the mid-cross-section, positioned 10 and 20 mm from the weld groove, respectively. The temperature recorder logged data every 0.5 s. In addition, the deformation of the test plate was measured using a lever-percentage meter with a measurement accuracy of 0.02 mm, as shown in Figure 4.

Figure 2 Multichannel temperature recorder

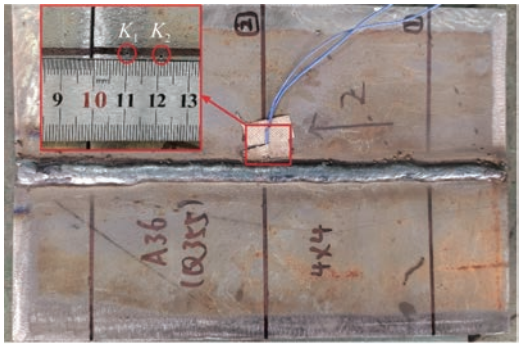

Figure 3 Experimental structure and temperature measurement points

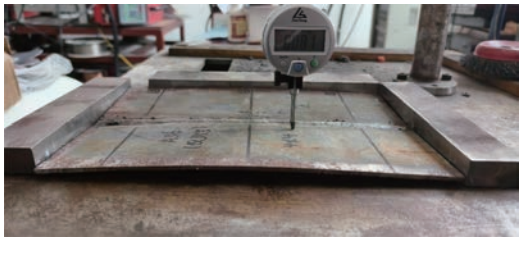

Figure 4 Experimental result and measurement

3 Numerical simulation methods

3.1 TEP-FEM

High-temperature fusion welding is a complex, multi-field, coupled, nonlinear process. Its complexity manifests

in various aspects: the heat source is locally applied relative to the overall component and is mostly mobile; the temperature field undergoes drastic changes. Further, the material properties, among others, vary significantly at different temperatures. Presently, the most commonly used method in this field is the nonlinear TEP-FEM. This approach can simulate the whole welding process, providing the temperature and stress-strain fields at every time point. From this perspective, the thermal elastic-plastic theory of welding includes both the temperature field theory and the stress-strain field theory (Chiocca et al., 2021; Ghafouri et al., 2022).

3.1.1 Thermal analysis

The sample is heated to a high temperature; the duration of high-temperature exposure is brief, and the cooling rate is rapid. Additionally, the temperature field undergoes rapid changes because the heat source moves. Hence, the temperature field falls into the category of transient heat conduction problems. The governing equation is as follows (Chiocca et al., 2021; Ghafouri et al., 2022):

$$\rho(T)c_{\mathrm{p}}(T)\frac{\partial T}{\partial t}=\frac{\partial}{\partial x}\left(k(T)\frac{\partial T}{\partial x}\right)+\frac{\partial}{\partial y}\left(k(T)\frac{\partial T}{\partial y}\right)+\frac{\partial}{\partial z}\left(k(T)\frac{\partial T}{\partial z}\right)+Q \tag{1}$$

where $\rho(T)$, $c_{\mathrm{p}}(T)$, and $k(T)$ represent the thermal-physical parameters, namely temperature-dependent density, specific heat capacity, and thermal conductivity, respectively. Q denotes the volume heat flux density (W/mm^3) from the internal heat source. The thermal-physical properties of the AH36 material related to temperature are illustrated in Figure 5 (Zhou et al., 2022; Gao, 2020). In the numerical simulation process, the base and filler materials were assumed to be the same material type.

The accuracy of the simulated temperature field depends greatly on the appropriate selection of a heat source model. For flux-cored arc welding (FCAW), the double ellipsoidal heat source model proposed by Goldak et al. (1984) (as shown in Figure 6) provides a more accurate representation of the actual weld pool morphology. This model employs two semiellipsoidal bodies of different dimensions at the leading and trailing sections to represent the heat input. The ensuing heat flux distribution is described by the following expression (Hashemzadeh et al., 2021; Hashemzadeh et al., 2022):

The heat flux condition within the first half of the ellipsoid $(y \geqslant 0)$ is represented as follows:

$$Q_{\mathrm{f}}(x,y,z,t)=\frac{6\sqrt{3}\left(f_{\mathrm{f}}\eta UI\right)}{ab_{\mathrm{f}}c\pi\sqrt{\pi}}\exp\left(-\frac{3x^2}{a^2}-\frac{3(y+vt)^2}{b_{\mathrm{f}}^2}-\frac{3z^2}{c^2}\right) \tag{2}$$

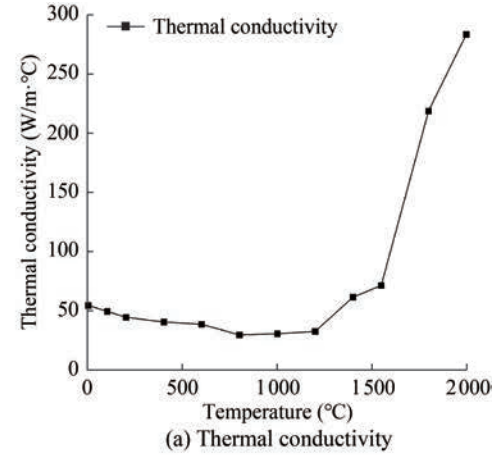

(a) Thermal conductivity

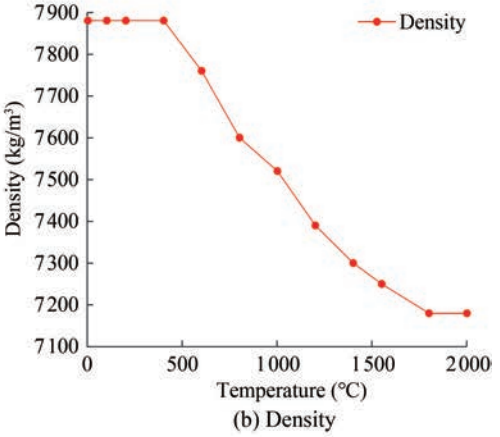

(b) Density

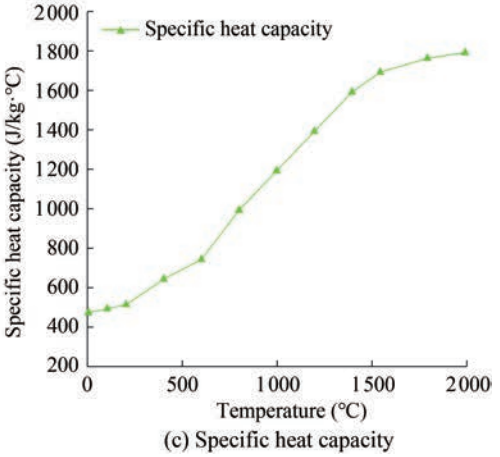

(c) Specific heat capacity

Figure 5 Temperature-dependent thermal-physical properties of AH36

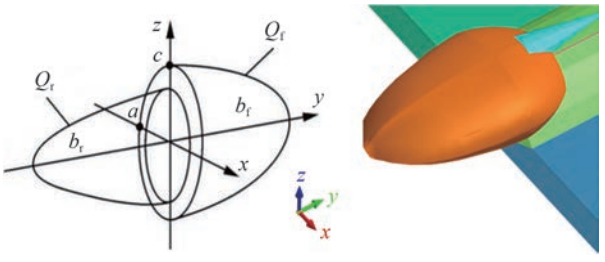

Figure 6 Double ellipsoidal heat source model

Here, η, the heat source efficiency, was set as 0.8; U stands for the welding voltage (V); I represents the welding current (A); a is half of the ellipsoid width; and c represents the depth of the ellipsoid; v denotes the welding speed (mm/s).

Meanwhile, the heat flux condition within the second half of the ellipsoid $(y < 0)$ can be expressed as follows:

$$Q_r(x,y,z,t) = \frac{6\sqrt{3}(f_r\eta UI)}{ab_r c\pi\sqrt{\pi}} \exp\left(-\frac{3x^2}{a} - \frac{3(y+vt)^2}{b_r^2} - \frac{3z^2}{c^2}\right) \quad (3)$$

Here, f_f and f_r represent the heat distribution functions, where $f_f + f_r = 2$; b_f and b_r are the lengths of the front and rear half-ellipsoids, respectively.

In the TEP-FEM numerical simulation, the applied thermal boundary conditions encompass both heat convection and heat radiation. The heat loss due to convection is governed by Newton's law of cooling (Hashemzadeh et al. 2022; Banik et al., 2021; Taraphdar et al., 2021):

$$q_c = -h_c(T_s - T_0) \quad (4)$$

where $h_c(=2.5\times10^{-5}\,\mathrm{W\cdot mm^{-2}\cdot K^{-1}})$ represents the heat transfer coefficient; T_s refers to the model surface temperature; and T_0(= 20 °C) is the environmental temperature.

The radiative heat transfer is governed by the Stefan-Boltzmann law (Hashemzadeh et al. 2022; Banik et al., 2021; Taraphdar et al., 2021):

$$q_r = -\sigma\varepsilon\left[(T_s + 273.15)^4 - (T_0 + 273.15)^4\right] \quad (5)$$

where $\sigma(=5.67\times10^{-8}\,\mathrm{W\cdot m^{-2}\cdot K^{-4}})$ refers to the Stefan–Boltzmann constant; $\varepsilon(=0.8)$ is the emissivity factor.

3.1.2 Mechanical analysis

In this investigation, the welding process was simulated via the TEP-FEM approach within a coupled thermal-metallurgical-mechanical multiphysics framework. The thermal analysis results were sequentially applied as initial mechanical loads within the same finite element model to compute the strain, displacement, and stress fields throughout the welding cycle (Hashemzadeh et al. 2022; Ghafouri et al., 2022). The temperature-dependent mechanical properties, as shown in Figure 7, were required to perform the mechanical calculations (Zhou et al., 2022; Gao, 2020). The impact of phase transformation on plasticity was considered in the mechanical calculations. Further, the elastic stress-strain association of the material was assumed to conform to Hooke's law, and the plastic feature to the Von Mises criterion. Accordingly, the stress-strain relationship can be described as follows (Ghafouri et al., 2022; Li et al., 2021):

$$[d_\sigma] = [\boldsymbol{D}^{ep}][d_\varepsilon] - [\boldsymbol{C}^{th}]\mathrm{d}T \quad (6)$$

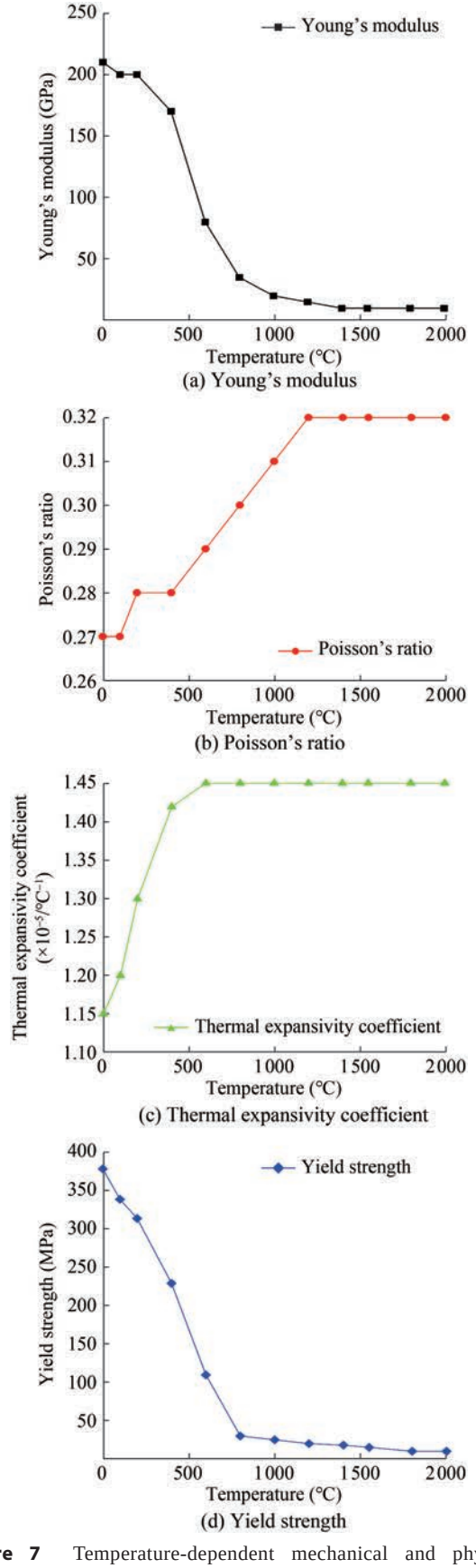

Figure 7 Temperature-dependent mechanical and physical performances of AH36

$$\left[\boldsymbol{D}^{\mathrm{ep}}\right] = \left[\boldsymbol{D}^{\mathrm{e}}\right] - \left[\boldsymbol{D}^{\mathrm{p}}\right] \tag{7}$$

Here, d_σ, d_ε, and dT denote the stress increment, strain increment, and temperature increment, respectively, and $\left[\boldsymbol{D}^{\mathrm{e}}\right]$, $\left[\boldsymbol{D}^{\mathrm{p}}\right]$, and $\left[\boldsymbol{C}^{\mathrm{th}}\right]$ are the elastic stiffness matrix, plastic stiffness matrix, and thermal stiffness matrix, respectively. Owing to the transient thermal exposure at each nodal point during welding, the total strain increment in the mechanical model can be decomposed into the following four components (Ghafouri et al., 2022; Li et al., 2021):

$$\Delta\varepsilon^{\mathrm{total}} = \Delta\varepsilon^{\mathrm{e}} + \Delta\varepsilon^{\mathrm{p}} + \Delta\varepsilon^{\mathrm{T}} + \Delta\varepsilon^{\mathrm{tr}} \tag{8}$$

where $\Delta\varepsilon^{\mathrm{total}}$, $\Delta\varepsilon^{\mathrm{e}}$, $\Delta\varepsilon^{\mathrm{p}}$, $\Delta\varepsilon^{\mathrm{T}}$ and $\Delta\varepsilon^{\mathrm{tr}}$ denote the total, elastic, plastic, thermal, and phase-transformation strain increments, respectively.

3.1.3 TEP-FEM finite element model creation and constraints

During the welding process, weld seam filling can be achieved using the quiet element method. This method requires a predefined weld seam mesh and treats the filled weld as a continuum. In numerical simulation, the quiet element does not affect the analysis results when in an inactive state. The element will be converted into an active element and participate in the computation only once its temperature exceeds the melting temperature (Jia et al., 2024). Considering the plate thickness and joint configuration used in the experiment, a 3D solid finite element model was established for numerical simulation. This model is shown in Figure 8, with the red arrow indicating the welding direction. Given that welding constitutes a nonuniform heating process, significant temperature gradients exist within the weld and its heat-affected zone. To ensure the accuracy of the analysis results while improving computational efficiency, a nonuniform transition mesh was employed to reduce the computational burden without compromising precision. In the finite element simulation model, a refined mesh was applied in the heat-affected zone (HAZ) to enhance computational accuracy, while a relatively coarser mesh was utilized in regions farther from the weld. To ensure the inclusion of multiple elements within a complete heat source model to meet precision requirements, the mesh size in the weld region was set to 3 mm in length and 1 mm in both height and width. The meshed finite element model consisted entirely of 8-node hexahedral elements of type 3 008, with a total of 19 200 3D elements and 23 331 nodes. During the actual welding process, the workpiece lacked external clamping. In mechanical calculations, predefined displacements at model nodes were set to zero (i.e., rigid constraints) to impede specific degrees of freedom, thereby preventing rigid translation and rotation of the finite element model.

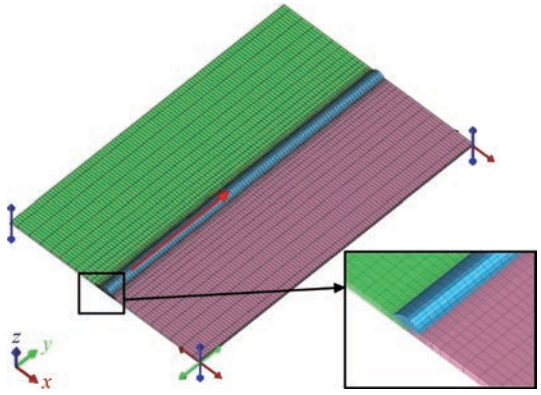

Figure 8 Thermal elastic-plastic finite element method (TEP-FEM) finite element model and constraints

3.2 ISM

For the ISM, it is not necessary to track the welding process at each moment. It focuses solely on the postweld deformation results. If the inherent strain magnitude and eccentricity of the weld seam are known and their relationship with welding parameters and plate dimensions is established, the inherent strain is applied as the initial strain to the corresponding regions of the weld seam and its heat-impacted region. Then, an elastic computation is performed to determine the welding deformation with the desired accuracy (Honaryar et al., 2020; Ueda et al., 1993; Ueda and Yuan, 1992; Liang et al., 2024). The principle of ISM for calculating welding deformation is depicted in Figure 9. In Figure 9, F_x and F_y represent the equivalent transverse shrinkage force and longitudinal shrinkage force caused by transverse and longitudinal weld contractions, respectively. M_x and M_y represent the equivalent transverse bending moment and longitudinal bending moment caused by transverse and longitudinal bending of the weld, respectively (Woo and Kitamura, 2022; Urbański and Taczała, 2022). Following the principle of ISM for calculating welding deformation, this method requires significantly less time to predict welding deformation compared to the nonlinear computation process of TEP-FEM.

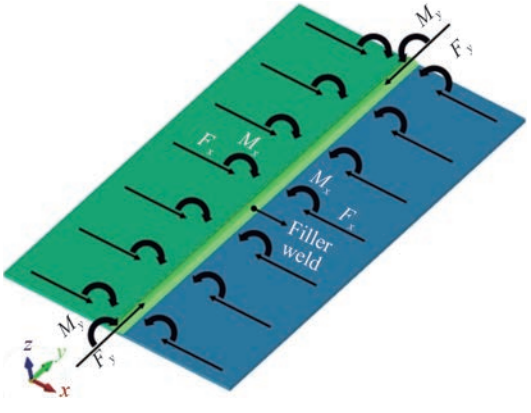

Figure 9 Schematic diagram of the principle for calculating welding deformation by the inherent strain method (ISM)

3.2.1 Inherent strain theory

Inherent strain represents the strain that remains in a structure after the weldment has been cycled through the heat of the weld. It is the source of internal stresses, which characterizes the strain produced when the material is in a free state after being dissected from the stress-containing state relative to the reference state. The total strain $\varepsilon^{\text{total}}$ in the welding process is decomposed into the elastic ε^{e}, plastic ε^{p}, thermal ε^{T}, creep ε^{c}, and transformation ε^{tr} strains, as shown below (Liang et al., 2024; Wu and Kim, 2020):

$$\varepsilon^{\text{total}} = \varepsilon^{e} + \varepsilon^{\text{p}} + \varepsilon^{\text{T}} + \varepsilon^{\text{c}} + \varepsilon^{\text{tr}} \tag{9}$$

When the weld is cooled to room temperature, the elastic strain is recovered, and the remaining inelastic strain is referred to as the inherent strain. Given that the transformation strain and creep strain have negligible effects on the final welding deformation, they can be disregarded. Furthermore, after a complete thermal cycle, the thermal strain also reduces to zero. Consequently, the final inherent strain is effectively equivalent to the residual plastic strain (Liang et al., 2024; Wu and Kim, 2020):

$$\varepsilon^{*} = \varepsilon^{\text{total}} - \varepsilon^{\text{e}} = \varepsilon^{\text{p}} \tag{10}$$

Then, the four main deformations of the welded member—transverse shrinkage δ_x^*, longitudinal shrinkage δ_y^*, transverse bending θ_x^*, and longitudinal bending θ_y^*—can be defined by the following equations (Liang et al., 2024; Urbański and Taczała, 2022):

$$\delta_x^* = \frac{1}{h}\iint \varepsilon_x^* \mathrm{d}x\mathrm{d}z \tag{11}$$

$$\delta_y^* = \frac{1}{h}\iint \varepsilon_y^* \mathrm{d}x\mathrm{d}z \tag{12}$$

$$\theta_x^* = \frac{12}{h^3}\iint \left(z - \frac{h}{2}\right)\varepsilon_x^* \mathrm{d}x\mathrm{d}z \tag{13}$$

$$\theta_y^* = \frac{12}{h^3}\iint \left(z - \frac{h}{2}\right)\varepsilon_y^* \mathrm{d}x\mathrm{d}z \tag{14}$$

where ε_x^* and ε_y^* denote the inherent strains in the transverse (perpendicular to the weld) and longitudinal (along the weld) directions, respectively; *x*, *y*, and *z* represent the directions perpendicular to welding, parallel to welding, and along the plate thickness, respectively; and *h* is the plate thickness.

3.2.2 Inherent strain acquisition and loading method

Currently, inherent strains are commonly obtained through experimental measurements, utilizing the existing inherent strain databases, and by employing TEP-FEM analysis to calculate inherent strains in typical welded joints (Wang et al., 2020; Ma et al., 2017). The results obtained in this study were compared with the TEP-FEM analysis results. Furthermore, TEP-FEM analysis is convenient for quantitatively analyzing the relationship between the distribution and magnitude of inherent strains and welding conditions. Hence, the TEP-FEM analysis was performed to obtain the magnitude and distribution of residual plastic strains—that is, inherent strain values.

During the numerical simulation, the inherent strain cannot be directly applied as an initial load to the weld and its adjacent region within the SYSWELD finite element software. Hence, an alternative approach is adopted whereby the inherent strain is indirectly introduced via a temperature-loading method by adjusting the thermal expansion coefficient of the material. This adjustment enables the simulation of specific welding-induced deformations. The modified thermal expansion coefficient can be determined using the following equation (Liang et al., 2024; Wu and Kim, 2020):

$$\varepsilon^{*} = \varepsilon^{\text{p}} = \alpha \cdot \Delta T \tag{15}$$

where ε^* is the inherent strain, defined as equivalent to the residual plastic strain; α denotes the thermal expansion coefficient of the material; and ΔT represents the temperature difference between the melting point of the material and the room temperature (ΔT was set to 1 430 ℃ in this study). Note that the default material database in SYSWELD does not support directionally dependent coefficients of thermal expansion. Therefore, the average residual plastic strain was utilized in this study.

3.2.3 Shell element finite element model creation and constraints

A shell element finite element model was established, as shown in Figure 10. To ensure accuracy and reliability, the same meshing scheme as that in the 3D solid finite element model was applied. Finer meshes were used in and around the weld seam, while coarser meshes were applied in regions farther from the weld seam. The shell element simulation model consists of 3 200 2D elements and 3 333 nodes. Compared to the 3D solid model in Figure 8, the shell element model has significantly fewer elements and nodes. Similarly, the boundary conditions of the shell element finite element model were consistent with those of the 3D solid model, ensuring that the plates could freely shrink in all directions without rotation. The shell element model and its boundary conditions are exhibited in Figure 10.

3.2.4 Principle of the temperature gradient-thermal strain method

In actual thin plate butt welding, which is depicted in Figure 11, there exists an eccentricity "e" between the bending neutral surface of the weldment (black line) and the center of the equivalent shrinkage force caused by the weldment (red dot). This eccentricity leads to the phenom-

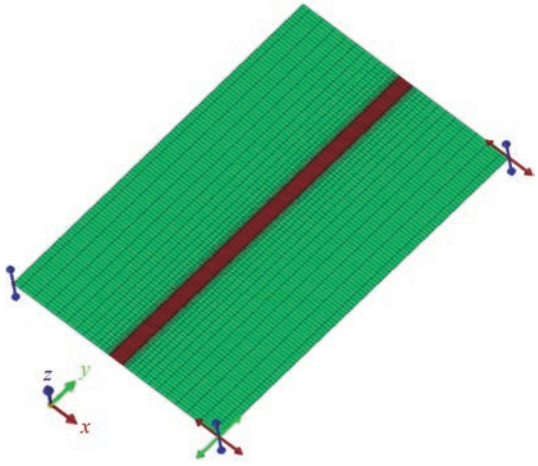

Figure 10 Shell element finite element model: model generation and constraints

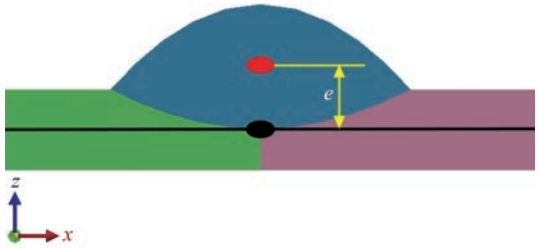

Figure 11 Schematic of the weld shrinkage force

ena of longitudinal bending deformation and transverse angular deformation after thin plate butt welding. The shell element finite element model, by default, lacks eccentricity. The welding deformation calculated directly using the inherent strain method results in in-plane longitudinal and transverse shrinkage, without any longitudinal bending deformation and transverse angular deformation. Out-of-plane longitudinal bending and angular deformation only occur when the bending neutral surface and the equivalent center of the longitudinal shrinkage force F_y and transverse shrinkage force F_x caused by the weld are not on the same plane. To ensure the efficient and accurate simulation of the actual welding deformation during butt welding using the shell element finite element model, this study proposes a method based on the temperature gradient principle, wherein different temperatures are applied in the thickness direction of the shell element. This principle is depicted in Figure 12. According to Equation (15), by applying a temperature difference ΔT across the thickness of the shell element, different inherent strains are generated in various thickness regions. This ensures that the neutral surface is not in the same plane as the equivalent center of the longitudinal and transverse shrinkage forces, and longitudinal bending deformation and transverse angular deformation are obtained. This method is referred to as the temperature gradient-thermal strain method (TG-TSM) in this study, where ΔT is given as follows:

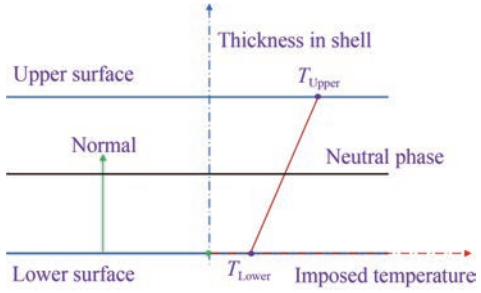

Figure 12 Temperature gradient principle based on shell element finite element modeling

$$\Delta T = T_{\text{upper}} - T_{\text{lower}} \tag{16}$$

where T_{upper} and T_{lower} are the temperatures of the upper and lower surfaces of the shell element model, respectively.

In TG-TSM, the plastic strain is obtained as a product of a constant thermal expansion coefficient α and a nonuniform temperature field in the shell element finite element model. This strain is the driving force for shrinkage deformation during the cooling phase of welding. Figure 13 illustrates the mechanism of inputting equivalent thermal strain in the shell element finite element model using the TG-TSM. The assumed thermal expansion coefficient α is equivalent to the inherent strain ε^* in the weld region. The resulting equivalent shrinkage force F^* and equivalent bending moment M^* are given as follows (Wang et al., 2021):

$$F_x^* = E \cdot \int \varepsilon_x^* \cdot b(z)\,\mathrm{d}z \tag{17}$$

$$F_y^* = E \cdot \int \varepsilon_y^* \cdot b(z)\,\mathrm{d}z \tag{18}$$

$$M_x^* = E \cdot \int \varepsilon_x^* \cdot b(z) \cdot z\,\mathrm{d}z \tag{19}$$

$$M_y^* = E \cdot \int \varepsilon_y^* \cdot b(z) \cdot z\,\mathrm{d}z \tag{20}$$

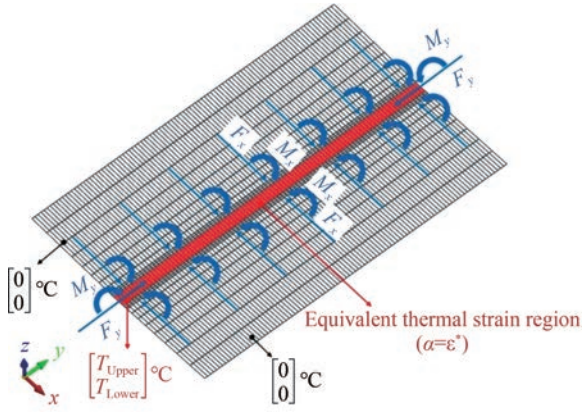

Figure 13 Schematic of the principle for calculating welding deformation by temperature gradient-thermal strain method (TG-TSM)

where F_x^* and F_y^* are the equivalent transverse and longitudinal shrinkage forces, respectively; M_x^* and M_y^* are the equivalent transverse and longitudinal bending moments,

respectively; ε_x^* and ε_y^* are the transverse and longitudinal inherent strains, respectively; E is the elastic modulus at room temperature; and $b(z)$ is the inherent strain width at the corresponding position.

4 Results and discussion

4.1 TEP-FEM simulation results

4.1.1 Welding temperature field simulation results

Using TEP-FEM along with a 3D solid finite element model, heat source calibration was performed based on the actual weld pool morphology and the measured thermal cycle curves at points K_1 and K_2. The numerically simulated temperature field obtained after multiple iterations and revisions of the heat source model is shown in Figure 14. The figure shows the temperature field distributions at 90 and 180 s, as well as a comparison between the simulated weld pool morphology and the actual weld pool morphology, demonstrating that the simulated weld pool shape is in good agreement with the actual one. Thermal cycle curves at positions K_1 and K_2 were simultaneously extracted and compared with the experimentally measured ones, as shown in Figure 15. The findings are as follows: First, the trends in the thermal cycle curves at both positions are consistent; as the heat source approaches K_1 and K_2, the temperature rises rapidly, and the temperature gradient in front of the heat source is greater than that behind it. Since K_2 is located further from the weld, its peak temperature is lower than that of K_1. Second, there are some temperature differences between the numerically simulated and experimentally obtained thermal cycle curves; however, these discrepancies mainly occur during the cooling process from 100 °C to room temperature and hence have minimal impact on subsequent mechanical calculations. Therefore, it can be concluded that the heat source model parameters selected in this study are reasonable and accurately reflect the actual shape of the heat source. The calibrated heat source model parameters are listed in Table 4.

4.1.2 Welding deformation and residual plastic strain distribution

The welding deformation calculated by the thermal-mechanical coupling method based on the temperature field obtained from the aforementioned computation is shown in Figure 16. Because of the action of compressive stresses in the plate on both sides caused by the peak longitudinal tensile stresses in the weld, the plate experiences buckling instability when the value of the compressive stresses is higher than the critical instability stress of the plate. In the longitudinal direction, the radius of curvature experiences bending deformation, and deflection exists. In the cross-section, the center of the weld is lower than the edge of the

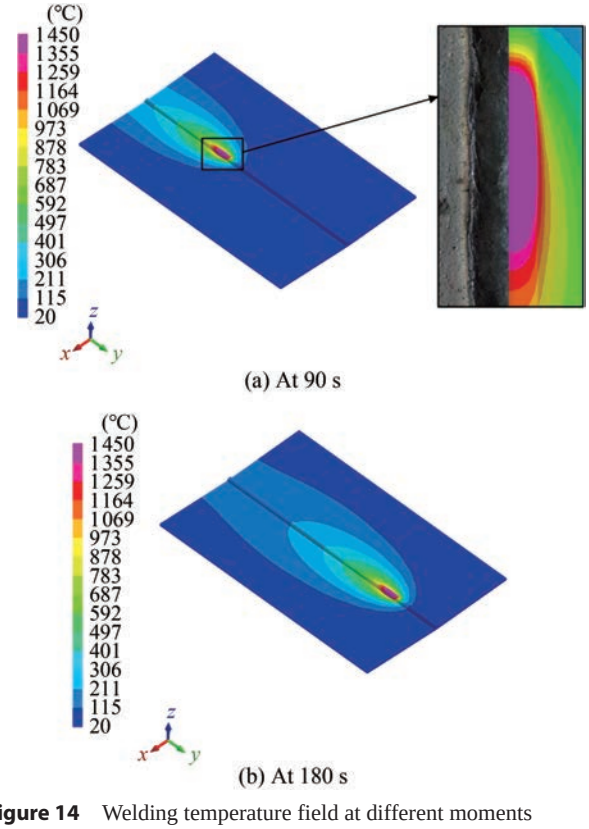

Figure 14 Welding temperature field at different moments

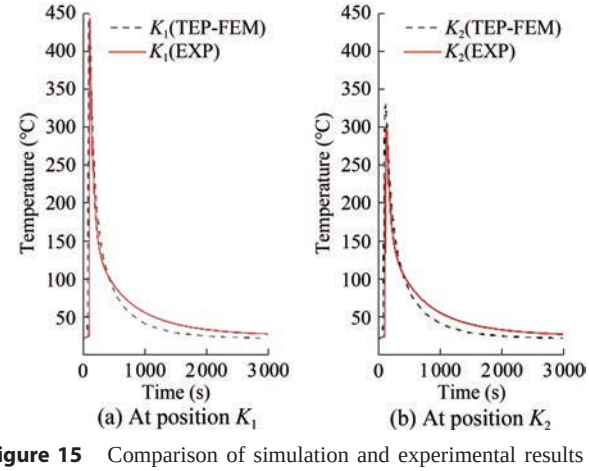

Figure 15 Comparison of simulation and experimental results for the welding temperature thermal cycle curves

Table 4 Double ellipsoidal heat source model parameters (mm)

a_f	a_r	b	c	f_f	f_r
8.33	16.67	6	3	1.1	0.9

plate because the residual stress field has a minimum potential energy in the steady state. The plate is destabilized by the residual compressive stress, which makes the point of action of the contraction force eccentric and produces the bending moment required for longitudinal bending, thereby intensifying the longitudinal deflection of the plate, finally producing saddle-shaped deformation. The deformation trend agrees with the experimental results of this study (as

shown in Figure 4) and the known theoretical characteristics of thin-plate butt welding distortion. Additionally, the residual plastic strain obtained by TEP-FEM is shown in Figure 17. Analysis indicates that residual plastic strain exists in the weld and HAZ, where the average value is computed to be 0.043.

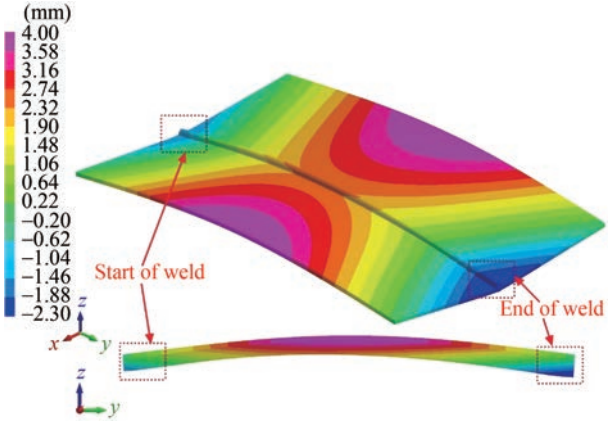

Figure 16 Welding deformation cloud obtained by TEP-FEM calculation (deformation scale: 2)

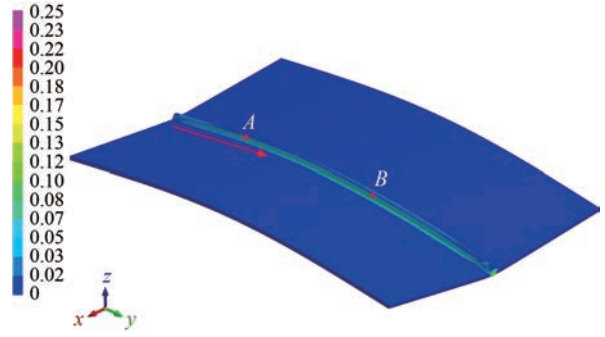

Figure 17 Residual plastic strain distribution obtained by TEP-FEM calculation (deformation scale: 2)

In this study, the temperature field calculated by the TEP-FEM was used to define the temperature difference ΔT. As shown in Figure 17, the residual plastic strain is mainly located in the weld and its HAZ. Therefore, the variation curves of the node-averaged temperature with time for the weld and its HAZ in the upper and lower parts of the neutral phase of the plate were calculated separately, as shown in Figure 18. As observed from this figure, the average temperature of the nodes in the upper part of the neutral phase during the welding process is approximately 250 °C higher than that of the nodes in the lower part. Considering the effect of weld reinforcement, the temperature difference ΔT was assumed to be 500 °C in this study.

4.2 TG-TSM simulation results

The average residual plastic strain in the weld and its surrounding areas, as calculated by TEP-FEM, was converted to the coefficient of thermal expansion using Equation (15). This coefficient was then applied to the corresponding region in the shell element finite element model, as shown in Figure 10. The TG-TSM method was then used for the calculation. The calculated welding deformation is shown in Figure 19, revealing a saddle-shaped deformation trend. Compared to the deformation contour obtained from TEP-FEM in Figure 16, both computational methods exhibit a saddle-shaped deformation. However, there are discrepancies between the two methods in terms of the welding deformation trends at the start and end of welding. Moreover, the welding deformation calculated by TG-TSM is significantly smaller than the TEP-FEM and experimental results.

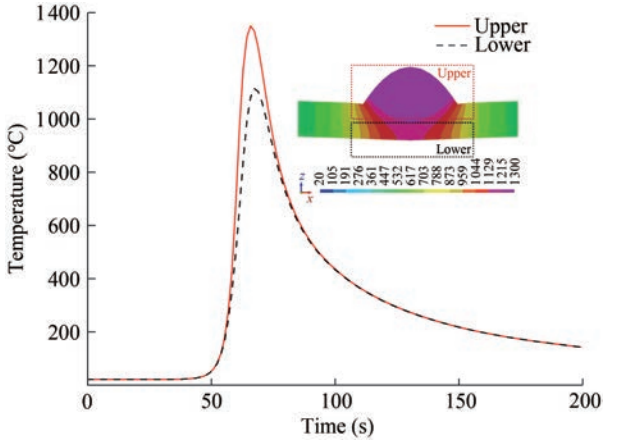

Figure 18 Variation curves of the node-averaged temperature with time

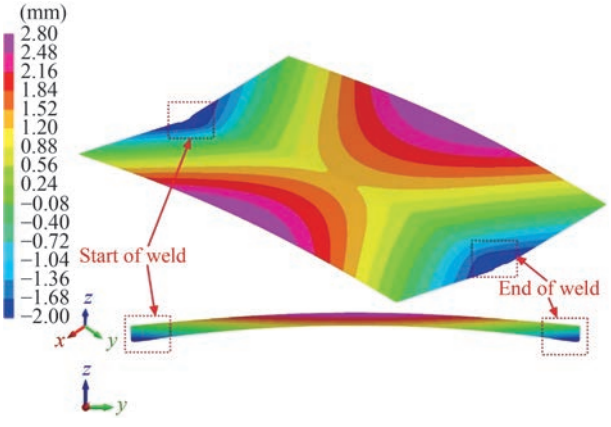

Figure 19 Welding deformation cloud obtained by TG-TSM calculation (deformation scale: 2)

4.3 Gradual temperature gradient-thermal strain method

The differences in the welding deformation calculated using TG-TSM (Figures 9 and 13) arise from the fact that this method applies the inherent strain to the corresponding weld region of the finite element model all at once. The welding deformation is then obtained through a single elas-

tic calculation. In fact, as shown in Figures 14 and 15, the heat source moves forward constantly during the welding process, and the tail of the heat source is rapidly cooled by thermal convection and thermal radiation, leading to the gradual solidification of the weld and thus a gradual shrinkage effect. To elaborate, the curve of plastic strain versus time at two selected points *A* and *B* (as shown in Figure 17; the red arrow indicates the welding direction) on the weld seam is shown in Figure 20. Time points P_A and P_B correspond to the moments when the weld at positions *A* and *B*, respectively, reaches stable plastic strain, also known as residual plastic strain. First, the onset of plastic strain occurs at different times for the welds at *A* and *B* during the welding process. Second, there exists a time difference between P_A, when the weld at *A* reaches its final residual plastic strain, and P_B, when the weld at *B* reaches its final residual plastic strain. This time difference arises because the weld at A occurs earlier, resulting in the formatting of the residual plastic strain earlier at *A* than at *B*.

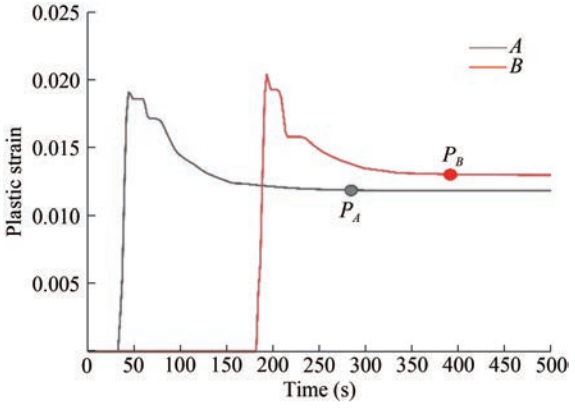

Figure 20 Plastic strain versus time curve for the weld at different positions

Consequently, the residual plastic strain within the weld and its HAZ develops progressively in the welding direction rather than simultaneously. However, the TG-TSM method does not account for the gradual accumulation of residual plastic strain that occurs during welding deformation simulation. This strain accumulation is the major source of discrepancy between the predictions and the results obtained from both experimental measurements and TEP-FEM simulations. To overcome this shortcoming of TG-TSM, this study proposes an improved approach involving the gradual application of residual plastic strain in the welding direction. This method, referred to as the GTG-TSM, simulates the time-dependent evolution of residual plastic strain during welding. The computational principle of GTG-TSM is shown in Figure 21.

The welding deformation results obtained by the GTG-TSM method, in conjunction with the parameters adopted for TG-TSM as described earlier, are shown in Figure 22. A comparison of Figure 22 with Figures 16 and 19 indicates that the deformation trend predicted by GTG-TSM agrees more closely (than TG-TSM) with that predicted by TEP-FEM. To further evaluate the discrepancies in the results of the three numerical methods in comparison with experimental measurements, longitudinal bending deformation and transverse angular deformation were extracted along longitudinal path L_1 and transverse paths T_1, T_2, and T_3, as defined in Figure 1. The comparison results are shown in Figure 23.

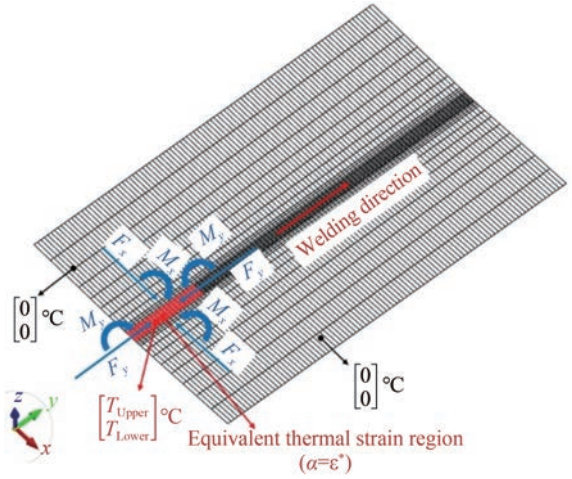

Figure 21 Schematic of the principle for calculating welding deformation by GTG-TSM

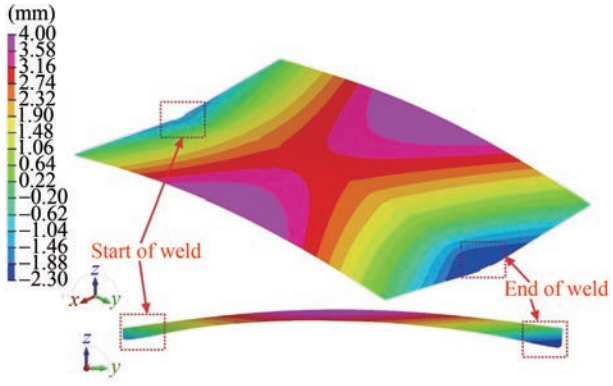

Figure 22 Welding deformation cloud obtained by the GTG-TSM calculation (deformation scale: 2)

The comparison of the transverse angular deformation at the three positions shown in Figure 23(a)–(c) reveals that the angular deformation calculated by TEP-FEM closely matches the experimental results, with a small error. In contrast, the angular deformation calculated by TG-TSM shows significant discrepancies at all three locations compared to both TEP-FEM and the experimental result, particularly in generating nearly identical angular deformations at the start and end of the weld. However, both the TEP-FEM and experimental results indicate that the angular deformation at the start of the weld is smaller than at the end. Furthermore, the angular deformation calculated by TG-TSM at the middle location differs significantly

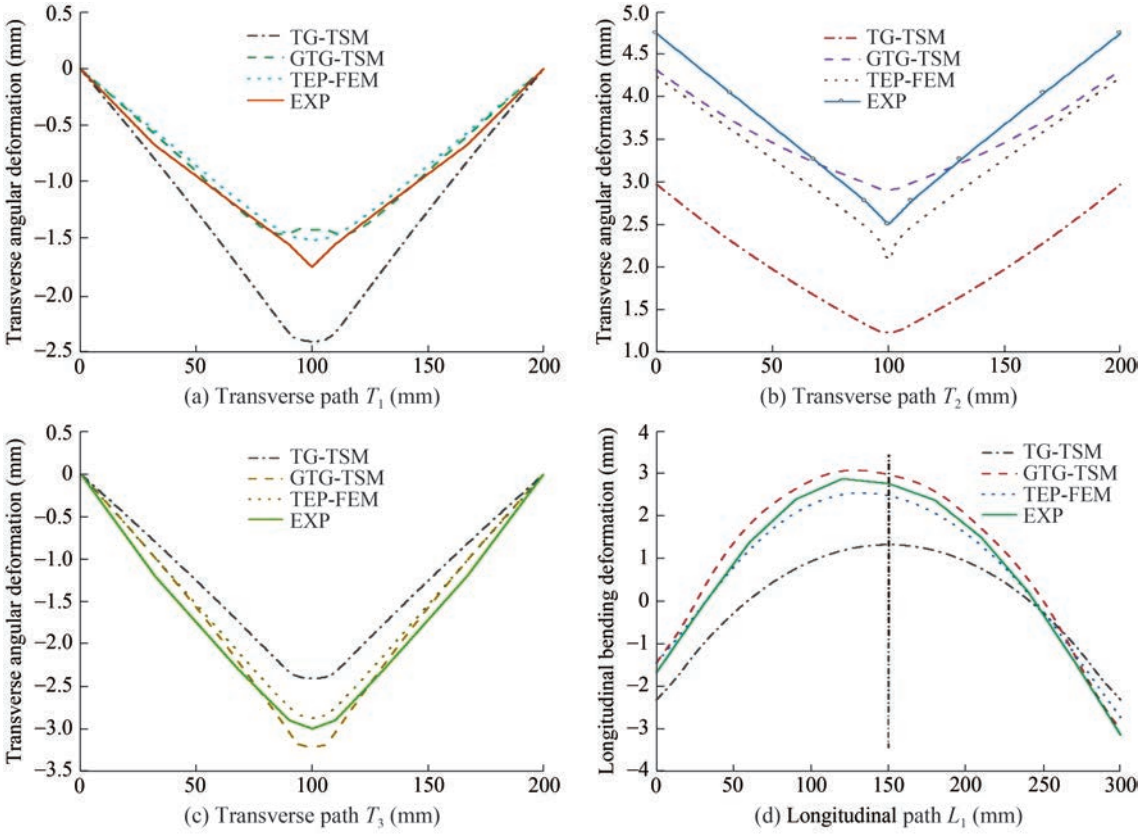

Figure 23 Comparison of the welding deformation result simulated by different numerical simulation methods with experimental results

from the experimental and TEP-FEM results. In comparison, the angular deformations at the three locations calculated using the GTG-TSM method proposed in this study are in good agreement with both the TEP-FEM and experimental results, with small errors in angular deformation at all positions compared to the experimental results.

In addition, as shown in Figure 23(d), a comparison of the longitudinal bending deformation caused by longitudinal shrinkage force indicates that the trend of the longitudinal bending deformation calculated by TEP-FEM is consistent with the experimental results, with a very small error. Although the longitudinal bending deformation calculated using TG-TSM is similar to the experimental and TEP-FEM results, both showing arching longitudinal bending deformation, the TG-TSM result exhibits a symmetric distribution of bending deformation centered around the mid-cross-section. In contrast, the experimental result and TEP-FEM calculation result show asymmetric bending deformation trends on either side of the mid-cross-section. Furthermore, the longitudinal bending deformation calculated using TG-TSM shows a large error and is significantly smaller than that of the experimental result. In contrast, the longitudinal bending deformation trend calculated by GTG-TSM is in good agreement with the TEP-FEM and experimental results, and the error is controlled within 10% compared with the experimental result.

4.4 Discussion

The primary cause for the significant discrepancy in the prediction results of the TG-TSM method compared to those of TEP-FEM and GTG-TSM lies in the fact that TG-TSM adopts a one-step loading approach. In this approach, the residual plastic strain is applied simultaneously to the entire weld and its surrounding area. Subsequently, a single elastic computation is performed to predict the welding deformation. In reality, however, the welding process involves a moving heat source that advances at a certain speed. The molten pool behind the heat source solidifies and contracts under the influence of thermal convection and radiation. Critically, the structural deformation induced by the solidification and contraction of the weld at an earlier stage affects the deformation caused by subsequent weld contraction. Consequently, the final welding deformation originates from the interaction and accumulation of residual plastic strains generated at different times. The TG-TSM method overlooks this gradual, time-dependent development of residual plastic strain during computation, resulting in considerable errors in its predictions compared to the TEP-FEM and GTG-TSM methods. In contrast, the GTG-TSM method gradually applies the residual plastic strain in the welding direction in the simulation. This incremental application more accurately mimics the actual generation process of residual plastic strain and accounts for

the influence of prior structural deformations on those occurring at later stages.

Thus, the GTG-TSM not only achieves a predictive accuracy comparable to that of TEP-FEM but also significantly reduces the computational time owing to its linear computational process, in contrast to the nonlinear nature of TEP-FEM. In this study, all three numerical simulation methods were executed on a quad-core processor, with the corresponding computation times shown in Figure 24. Although GTG-TSM requires more time than TG-TSM, it achieves a prediction accuracy similar to TEP-FEM with only 6% of the computation time. Furthermore, the shell-element-based finite element model simplifies model construction and markedly reduces the number of elements and nodes compared to a 3D solid-element model, leading to additional computational savings. Therefore, in terms of both accuracy and efficiency, GTG-TSM combined with a shell-element model is better suited for predicting the welding deformation in large-scale, complex, thin-walled structures.

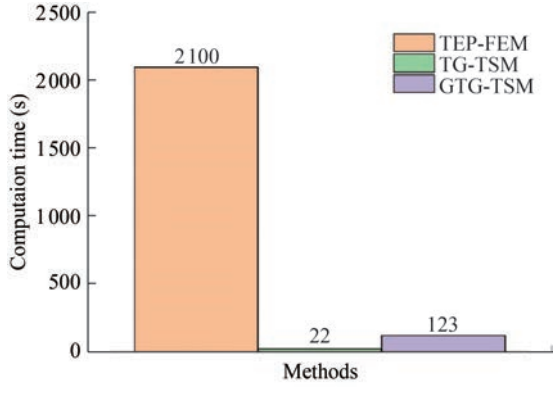

Figure 24 Comparison of the calculation times of the three methods

5 Conclusions

This study aimed to address the problem of efficient and accurate numerical simulation of butt welding deformation in marine thin plates. Toward this end, TG-TSM based on the inherent strain theory was proposed. This method does not consider the welding residual stress. The TEP-FEM, combined with a 3D solid finite element model, and TG-TSM of two computational forms, combined with a shell element finite element model, were used to numerically simulate the deformation of AH36 marine thin plate butt welding. By comparing and analyzing the model results with the experimental measurements, the following conclusions were drawn:

1) Although the TEP-FEM can accurately simulate the welding deformation of AH36 marine thin plate butt joints, its complex computational process results in long calculation times. Hence, this method cannot meet the practical production demands for efficient and accurate prediction of welding deformation in large and complex thin-plate structures.

2) The proposed TG-TSM, combined with a shell element finite element model, can numerically simulate the saddle-shaped deformation trend resulting from the butt welding of marine thin plates.

3) The GTG-TSM conforms to the formation law of residual plastic strain in the actual welding process. Therefore, the deformation result of the AH36 marine thin plate butt welding calculated by this method has a small error compared with the experimental result.

4) The accuracy of the GTG-TSM in predicting welding deformation is comparable to that of the TEP-FEM, with significantly lower computation time. Thus, the GTG-TSM is an effective tool for efficiently and accurately predicting welding deformation of large and complex thin-walled structures.

Funding Supported by the National Natural Science Foundation of China under Grant No. 51975138, the High-Tech Ship Scientific Research Project from the Ministry of Industry and Information Technology under Grant No. CJ05N20, and the National Defense Basic Research Project under Grant No. JCKY2023604C006.

Competing interests The authors have no competing interests to declare that are relevant to the content of this article.

References

Azad N, Iranmanesh M, Rahmati Darvazi A (2020) A study on the effect of welding sequence on welding distortion in ship deck structure. Ships and Offshore Structures 15(4): 355-367. https://doi.org/10.1080/17445302.2019.1619898

Banik S D, Kumar S, Singh PK, Bhattacharya S, Mahapatra MM (2021) Distortion and residual stresses in thick plate weld joint of austenitic stainless steel: Experiments and analysis. Journal of Materials Processing Technology 289: 116944. https://doi.org/10.1016/j.jmatprotec.2020.116944

Battista FR, Ambrogio G, Giorgini L, Guerrini M, Costantino S, Ricciardi F, Filice L (2024) Prediction of the keyhole TIG welding-induced distortions on Inconel 718 industrial gas turbine component by numerical-experimental approach. The International Journal of Advanced Manufacturing Technology 134: 4593-4608. https://doi.org/10.1007/s00170-024-14333-w

Chiocca A, Frendo F, Bertini L (2021) Evaluation of residual stresses in a pipe-to-plate welded joint by means of uncoupled thermal-structural simulation and experimental tests. International Journal of Mechanical Sciences 199: 106401. https://doi.org/10.1016/j.ijmecsci.2021.106401

Doan DS, Zden T (2021) Optimization of welding application parameters of thin sheet blocks used in the new generation ship hull. Emerging Materials Research 11(1): 67-75. https://doi.org/10.1680/jemmr.20.00330

Farajkhah V, Liu Y, Gannon L (2017) Finite element study of 3D simulated welding effect in aluminium plates. Ships and Offshore Structures 12(2): 196-208. https://doi.org/10.1080/17445302.2015.1123865

Gao J (2020) Research on the process of AH36 ship steel by laser arc hybrid welding. Nanjing: Nanjing University of Science and Technology. https://link.cnki.net/doi/10.27241/d.cnki.gnjgu.2020.000719

Gannon L, Liu Y, Pegg N, Smith MJ (2016) Nonlinear collapse analysis of stiffened plates considering welding-induced residual stress and distortion. Ships and Offshore Structures 11(3): 228-244. https://doi.org/10.1080/17445302.2014.985428

Ghafouri M, Ahola A, Ahn J, Björk T (2022) Numerical and experimental investigations on the welding residual stresses and distortions of the short fillet welds in high strength steel plates. Engineering Structures 260: 114269. https://doi.org/10.1016/j.engstruct.2022.114269

Goldak J, Chakravarti A, Bibby M (1984) A new finite element model for welding heat sources. Metallurgical Transactions B 15: 299-305. https://doi.org/10.1007/BF02667333

Hashemzadeh M, Garbatov Y, Guedes Soares C (2021) Welding-induced residual stresses and distortions of butt-welded corroded and intact plates. Marine Structures 79: 103041. https://doi.org/10.1016/j.marstruc.2021.103041

Hashemzadeh M, Garbatov Y, Guedes Soares C (2022) Hybrid-laser welding-induced distortions and residual stresses analysis of large-scale stiffener panel. Ocean Engineering 245: 110411. https://doi.org/10.1016/j.oceaneng.2021.110411

Honaryar A, Iranmanesh M, Liu P, Honaryar A (2020) Numerical and experimental investigations of outside corner joints welding deformation of an aluminum autonomous catamaran vehicle by inherent strain/deformation FE analysis. Ocean Engineering 200: 106976. https://doi.org/10.1016/j.oceaneng.2020.106976

Jia Y, Naceur H, Saadlaoui Y, Dubar L, Bergheau JM (2024) A comprehensive comparison of modeling strategies and simulation techniques applied in powder-based metallic additive manufacturing processes. Journal of Manufacturing Processes 110: 1-29. https://doi.org/10.1016/j.jmapro.2023.12.048

Li S, Hu L, Dai P, Bi T, Deng D (2021) Influence of the groove shape on welding residual stresses in P92/SUS304 dissimilar metal butt-welded joints. Journal of Manufacturing Processes 66: 376-386. https://doi.org/10.1016/j.jmapro.2021.04.030

Liang W, Mao Z, Hu L, Deng D (2024) Estimating welding deformation of ultra-thin mild steel bead-on-plate joints by means of inherent strain method. Thin-Walled Structures 199: 111825. https://doi.org/10.1016/j.tws.2024.111825

Lu Y, Lu C, Zhang D, Chen T, Zeng J, Wu P (2019) Numerical computation methods of welding deformation and their application in bogie frame for high-speed trains. J Manuf Process 38: 204-213. https://doi.org/10.1016/j.jmapro.2019.01.013

Ma N, Tateishi J, Hiroi S, Kunugi A, Huang H (2017) Fast prediction of welding distortion of large structures using inherent deformation database and comparison with measurement. Quarterly Journal of the Japan Welding Society 35: 137s-140s. https://doi.org/10.2207/qjjws.35.137s

Mancini F, Remes H, Romanoff J, Gallo P (2021) Influence of weld rigidity on the non-linear structural response of beams with a curved distortion. Engineering Structures 246: 113044. https://doi.org/10.1016/j.engstruct.2021.113044

Murakawa H, Luo Y, Ueda Y (2009) Prediction of welding deformation and residual stress by elastic fem based on inherent strain. Journal of the Society of Naval Architects of Japan 1996 (180): 739-751. https://doi.org/10.2534/jjasnaoe1968.1996.180_739

Nishimura R, Ma N, Liu Y, Li W, Yasuki T (2021) Measurement and analysis of welding deformation and residual stress in CMT welded lap joints of 1180 MPa steel sheets. Journal of Manufacturing Processes 72: 515-528. https://doi.org/10.1016/j.jmapro.2021.10.050

Qiu Y, Yan R, Wang N, Shen W, Xu S, Li M, Qin K (2023) Stress amplification effect and fatigue strength evaluation of marine thin plate welded structure considering welding deformation: Theoretical and experimental analysis. Thin-Walled Structures 188: 110871. https://doi.org/10.1016/j.tws.2023.110871

Shoor S, Shoor R, Dhiman R, Singh M, Sharma S, Kumar A, Singh R, Abbas M (2024) Experiment and FEA simulation for predicting maximum distortion in the submerged arc welding process. International Journal on Interactive Design and Manufacturing 18: 3887-3907. https://doi.org/10.1007/s12008-024-01820-3

Su Y, Yang X, Wu D, Meng T, Li W, Feng W, Vairis A (2023) Optimizing welding sequence of TIG cross-joint of Invar steel using residual stresses and deformations. Journal of Manufacturing Processes 105: 232-245. https://doi.org/10.1016/j.jmapro.2023.09.047

Taraphdar PK, Kumar R, Giri A, Pandey C, Mahapatra MM, Sridhar K (2021) Residual stress distribution in thick double-V butt welds with varying groove configuration, restraints and mechanical tensioning. Journal of Manufacturing Processes 68: 1405-1417. https://doi.org/10.1016/j.jmapro.2021.06.046

Ueda Y, Yamakawa T (1971) Analysis of thermal elastic-plastic stress and strain during welding by finite element method. Japan Welding Society Transactions 2(2): 90-100

Ueda Y, Yuan MG, Mochizuki M, Umezawa S, Enomoto K (1993) Experimental verification of a method for prediction of welding residual stresses in T joints using inherent strains 4th report: Method for prediction using source of residual stress. Welding International 7: 863-869. https://doi.org/10.1080/09507119309548506

Ueda Y, Yuan MG (1992) Prediction of welding residual stresses in T and I joints using inherent strains. 3rd report: Method for prediction of welding residual stress using residual stress generation source. Welding International 6(4): 263-269. https://doi.org/10.1080/09507119209548183

Urbański T, Taczała M (2022) Prediction of the welding distortions of butt welded joints using total moments method based on equivalent loads. Journal of Manufacturing Processes 75: 1039-1057. https://doi.org/10.1016/j.jmapro.2022.01.053

Wang J, Shi X, Zhou H, Yang Z, Liu J (2020) Dimensional precision controlling on out-of-plane welding distortion of major structures in fabrication of ultra large container ship with 20000TEU. Ocean Engineering 199: 106993. https://doi.org/10.1016/j.oceaneng.2020.106993

Wang C, Pham DT, Wu C, Kim JW, Su S, Jin Z (2021) Artificial thermal strain method: A novel approach for the analysis and fast prediction of the thermal distortion. Journal of Materials Processing Technology 289: 116937. https://doi.org/10.1016/j.jmatprotec.2020.116937

Woo D, Kitamura M (2022) Optimal simultaneous welding to minimise welding deformation of a general ship grillage structure. Ships and Offshore Structures 17(2): 268-278. https://doi.org/10.1080/17445302.2020.1827638

Wu C, Kim JW (2020) Numerical prediction of deformation in thin-plate welded joints using equivalent thermal strain method. Thin-Walled Structures 157: 107033. https://doi.org/10.1016/j.tws.2020.107033

Zhou H, Yi B, Shen C, Wang J, Liu J, Wu T (2022) Mitigation of welding induced buckling with transient thermal tension and its application for accurate fabrication of offshore cabin structure. Marine Structures 81: 103104. https://doi.org/10.1016/j.marstruc.2021.103104